Frequency-domain optical imaging of absorption and scattering distributions by a Born iterative method

Yuqi Yao and Yao Wang

Department of Electrical Engineering, Polytechnic University, Brooklyn, New York 11201

Yaling Pei

Department of Civil Engineering, Polytechnic University, Brooklyn, New York 11201

Wenwu Zhu

Department of Electrical Engineering, Polytechnic University, Brooklyn, New York 11201

Randall L. Barbour

Departments of Pathology and of Physiology and Biophysics, State University of New York Health Science Center, Brooklyn, New York 11203

We present a Born iterative method for reconstructing optical properties of turbid media by means of frequency-domain data. The approach is based on iterative solutions of a linear perturbation equation, which is derived from the integral form of the Helmholtz wave equation for photon-density waves. In each iteration the total field and the associated weight matrix are recalculated based on the previous reconstructed image. We then obtain a new estimate by solving the updated perturbation equation. The forward solution, also based on a Helmholtz equation, is obtained by a multigrid finite difference method. The inversion is carried out through a Tikhonov regularized optimization process by the conjugate gradient descent method. Using this method, we first reconstruct the distribution of the complex wave numbers in a test medium, from which the absorption and the scattering distributions are then derived. Simulation results with two-dimensional test media have shown that this method can yield quantitatively (in terms of coefficient values) as well as qualitatively (in terms of object location and shape) accurate reconstructions of absorption and scattering distributions in cases in which the first-order Born approximation cannot work well. Both full-angle and limited-angle measurement schemes have been simulated to examine the effect of the location of detectors and sources. The robustness of the algorithm to noise has also been evaluated. © 1997 Optical Society of America. [S0740-3232(97)02501-5]

1. INTRODUCTION

Optical measurements in the frequency domain have been used to study bulk photon propagation[1–5] and to image objects[6–10] in highly scattering media such as human tissue. Results from these studies support the idea that such measurements may prove a useful diagnostic tool for early detection of tumors. The imaging problem entails the reconstruction of the absorption and the scattering coefficients of an inhomogeneous scattering medium from measurement of multiple scattered light signals on the medium surface. This is an inverse scattering problem. This problem is difficult because the scattered field is nonlinearly related to the properties of the medium and because scattering occurs randomly and cannot be neglected for objects with strong contrast. These properties make it impossible to derive a closed-form expression. In the past, either the Born or the Rytov approximation has been utilized to linearize the problem.[11–12] However, this approximation is not valid in the presence of strong perturbations, i.e., when the absorption or the scattering coefficients of the actual medium are significantly different from those of a specified background. More general iterative perturbation approaches have been described in Refs. 7, 9, 13, and 14, which iteratively update and solve a linear perturbation equation. The perturbation equations in these studies are derived based on the first-order Taylor approximation of the detected signal. These equations linearly relate the changes in the detector readings (data) and the changes in the medium properties (the unknown image) from a previous estimate (the background medium) through a Jacobian matrix, which is more often referred to as the weight matrix in optical tomography literature. Each iteration of the perturbation approach essentially consists of two steps: The forward step updates the detector signal and the Jacobian matrix based on the previous solution of the unknown image, whereas the inverse step solves the updated perturbation equation to yield a new estimate of the unknown image.

The approaches reported in Refs. 7 and 9 are derived based on the diffusion approximation, whereas those in Ref. 13 are based on the transport model.

An alternative way of setting up the perturbation equation is to discretize the integral form of the wave equation or the diffusion equation. In fact, this type of approach has been explored previously for the electromagnetic inverse scattering problem. In Refs. 15–17 the so-called Born iterative method (BIM) and the distorted Born iterative method (DBIM) have been used successfully to solve nonlinear two-dimensional (2D) profile inversions, using both single-frequency and time-domain data. The DBIM is equivalent to the Newton–Kantorovich method. Joachimowicz *et al.*[18] have also proposed an algorithm based on the Newton–Kantorovich method for reconstructing objects whose dielectric properties are similar to those of biological tissues. In such formulations the elements in the weight matrix consist of the product of the Green's function for a background medium and the total field for the actual medium. In the BIM the background medium is fixed, and only the total field is updated based on the previous estimate of the medium. In the DBIM the background medium is continuously updated to be the newly estimated target medium. Consequently, both the Green's function and the total field also need to be updated. It has been observed that the DBIM converges faster than the BIM but that it is less robust to noise than is the BIM.

In this paper we apply the BIM to solve for the absorption and the scattering coefficients of a turbid medium under optical illumination. The approach is derived based on the integral form of the Helmholtz wave equation. Starting with a chosen homogeneous background field, we employ the Born approximation to derive an initial linear perturbation equation, which is then solved to yield the first image. In each of the successive iterations, the total field and the associated weight matrix are recomputed based on the previous reconstructed image. A new estimate is then obtained by solution of the updated perturbation equation. This method is evaluated for several 2D test media containing objects having relatively large contrast compared with the background. The results show that accurate reconstructions can be achieved within a small number (less than 15 in our examples) of iterations. Reconstruction examples from both full-angle and limited-angle measurements are presented to show the effect of the source and the detector location on reconstruction accuracy. The robustness of the proposed algorithm to noise has been evaluated by addition of noise to simulated data. It is shown that quite accurate results can be obtained at a signal-to-noise ratio (SNR) as low as 25 dB.

2. FORWARD SOLUTION

A. Diffusive Light Transport in Turbid Media

The migration of near-infrared photons in a turbid medium Ω can be modeled with the diffusion theory.[19,20] Let $\mu_a(\mathbf{r})$ and $\mu_s{}'(\mathbf{r})$ represent the absorption and the equivalent isotropic scattering coefficients in a medium, respectively, and $D(\mathbf{r}) = \{3[\mu_a(\mathbf{r}) + \mu_s{}'(\mathbf{r})]\}^{-1}$ represent the diffusion coefficient. In general, these quantities are position dependent. The frequency-domain diffusion

equation for the fluence rate $u(\mathbf{r})$, which is due to a sinusoidally intensity-modulated point source of light, is given by[1]

$$\nabla \cdot [D(\mathbf{r})\nabla u(\mathbf{r})] + [-\mu_a(\mathbf{r}) + i(\omega/v)]u(\mathbf{r}) = -Q(\mathbf{r})$$

$$\mathbf{r} \in \Omega, \quad (1)$$

where v is the speed of light in the media and $Q(\mathbf{r})$ represents the source signal. By means of the identity $\nabla \cdot [D(\mathbf{r})\nabla u(\mathbf{r})] = D(\mathbf{r})\nabla^2 u(\mathbf{r}) + \nabla u(\mathbf{r}) \cdot \nabla D(\mathbf{r})$, Eq. (1) becomes

$$\nabla^2 u(\mathbf{r}) + k^2(\mathbf{r})u(\mathbf{r}) = -S(\mathbf{r}) - \frac{\nabla u(\mathbf{r}) \cdot \nabla D(\mathbf{r})}{D(\mathbf{r})}, \quad (2)$$

where

$$k(\mathbf{r}) = [-\mu_a(\mathbf{r})/D(\mathbf{r}) + i\omega/vD(\mathbf{r})]^{1/2} \quad (3)$$

is referred to as the complex wave number and $S(\mathbf{r}) = Q(\mathbf{r})/D(\mathbf{r})$. In this paper we assume that the absorption and the scattering properties change smoothly, so that $\nabla D(\mathbf{r})$ is small. Under this condition, the second term of the right-hand side of Eq. (2) can be neglected. Then Eq. (2) becomes

$$\nabla^2 u(\mathbf{r}) + k^2(\mathbf{r})u(\mathbf{r}) = -S(\mathbf{r}). \quad (4)$$

Equation (4) can be solved numerically as a boundary-value problem, with the Dirichlet condition $u(\mathbf{r}) = 0$ on the boundary and with $u(\mathbf{r}) = S(\mathbf{r})$ at the source location, $\mathbf{r}_s$. Different numerical methods, such as the finite element[21] and the finite difference[9] methods, can be used to solve Eq. (4). Both can be implemented in a multigrid scheme to reduce computation time. The multigrid finite difference (MGFD) method used here is described below.

B. Multigrid Finite Difference Method

To solve Eq. (4) for a three-dimensional (3D) domain Ω, the finite difference method partitions the domain Ω into small volume elements (voxels) and approximates the differential operator by finite differences. This leads to

$$\frac{u_{i+1,j,k} + u_{i-1,j,k}}{\Delta x^2} + \frac{u_{i,j+1,k} + u_{i,j-1,k}}{\Delta y^2}$$

$$+ \frac{u_{i,j,k+1} + u_{i,j,k-1}}{\Delta z^2} - \left(\frac{2}{\Delta x^2} + \frac{2}{\Delta y^2} + \frac{2}{\Delta z^2}\right.$$

$$\left. - k_{i,j,k}^2\right)u_{i,j,k} = -S_{i,j,k}, \quad (5)$$

where i, j, and k are the indices for axes x, y and z, respectively; Δx, Δy, and Δz are the mesh sizes in the x, y, and z directions, respectively; and $k_{i,j,k} = k(i\Delta x, j\Delta y, k\Delta z) = (-\mu_{a_{i,j,k}}/D_{i,j,k} + i\omega/vD_{i,j,k})^{1/2}$, with $D_{i,j,k} = D(i\Delta x, j\Delta y, k\Delta z)$, $\mu_{a_{i,j,k}} = \mu_a(i\Delta x, j\Delta y, k\Delta z)$.

Equation (5) can also be denoted

$$Lu = f, \quad (6)$$

where the operator L depends on the medium properties $k_{i,j,k}$ and f depends on the source distribution. Rather than directly solving $u_{i,j,k}$ at the desired fine-grid level, the multigrid method solves u from a coarse grid to the
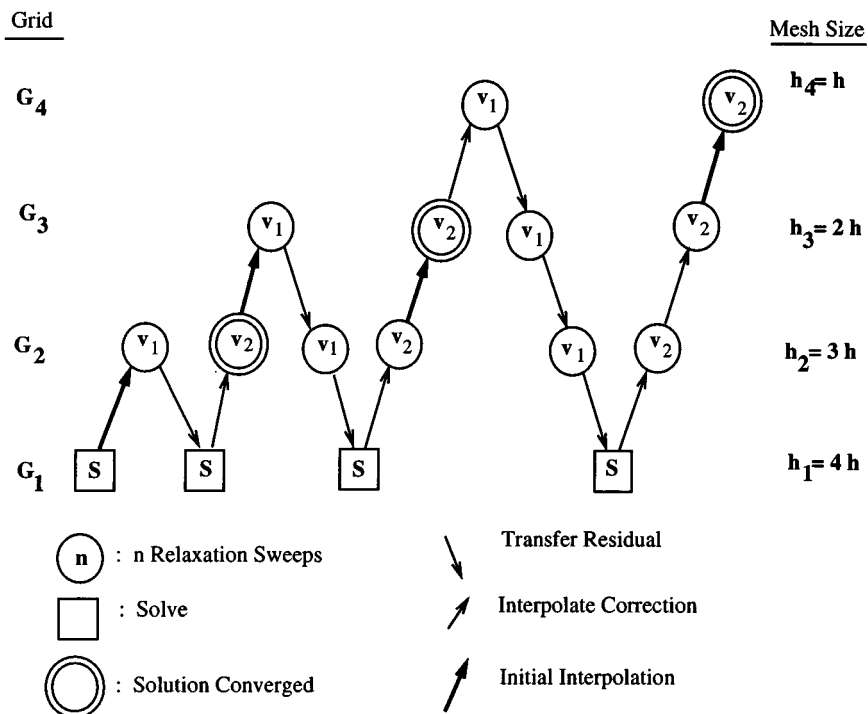
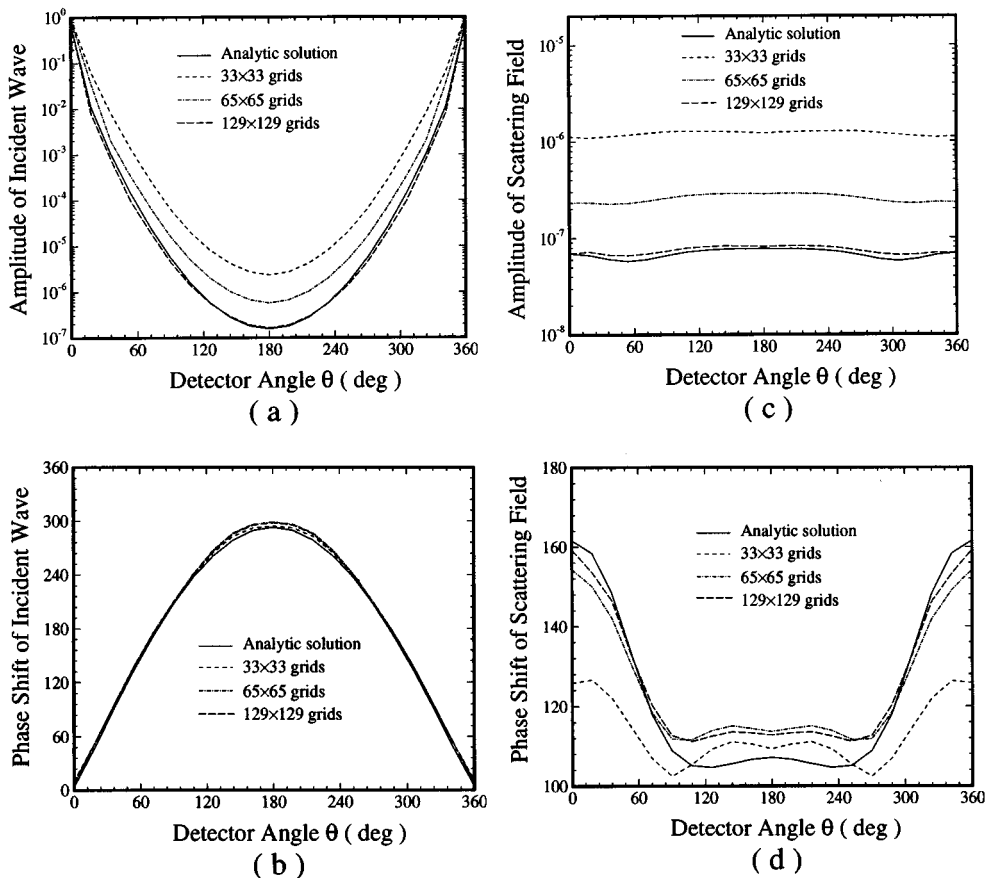Fig. 1. Full multigrid algorithm for a problem with $M = 4$ grids.

Fig. 2. (a) Amplitude and (b) phase shift of the incident wave obtained with different grid sizes in a 10 cm $\times$ 10 cm homogeneous medium with $\mu_a^b = 0.05$ cm^{-1} and $\mu_s'^b = 10.0$ cm^{-1}. (c) Amplitude and (d) phase shift of the scattered field obtained with different grid spacings, caused by a 0.7-cm-radius object, with $\mu_a = 0.2$ cm^{-1} and $\mu_s' = 30.0$ cm^{-1}. The modulation frequency is 200 MHz.

fine grid progressively. Among several multigrid schemes we use the full multigrid method.[22–25] Letting the number of grid levels be denoted by M, we write the equation solved at grid level k as

$$L^k u^k = f^k \quad k = 1, 2, \ldots, M. \tag{7}$$

At the finest grid $(k = M)$, $L^M = L$, $u^M = u$, $f^M = f$. The operators on the coarse grids are defined recursively from the original operator according to

$$L^{k-1} = (I_{k-1}{}^k)^T L^k I_{k-1}{}^k, \tag{8}$$

where $I_{k-1}{}^k$ is the coarse-to-fine operator from grid $k - 1$ to k by means of multilinear interpolation and $(I_{k-1}{}^k)^T$ is the reverse, fine-to-coarse, operator from grid k to $k - 1$. The source term on the $(k - 1)$th grid is given by

$$f^{k-1} = (I_{k-1}{}^k)^T r^k, \tag{9}$$

where

$$r^k = f^k - L^k u^k \tag{10}$$

Given: $k_b^2(r_j), u(r_{s_i}, r_{d_i})$

Forward Calculation:
$k_b^2(r_j) \rightarrow G(r_{d_i}, r_j), u_b(r_{si}, r_j), u_s = u - u_b$

Multigrid Method

$\hat{k}^2(r_j) \leftarrow k_b^2(r_j)$

Forward Calculation:
$\hat{k}^2(r_j) \rightarrow \hat{u}(r_{s_i}, r_j)$

Multigrid Method

$\|\hat{u} - u\|^2 \leq \epsilon?$ → **END**

Weight Update:
$\hat{u}(r_j), G(r_{d_i}, r_j) \rightarrow W_{ij}$

Inverse Calculation:
$W_{ij}, u_s(r_{s_i}, r_{d_i}) \rightarrow O(r_j) \rightarrow \hat{k}^2(r_j)$
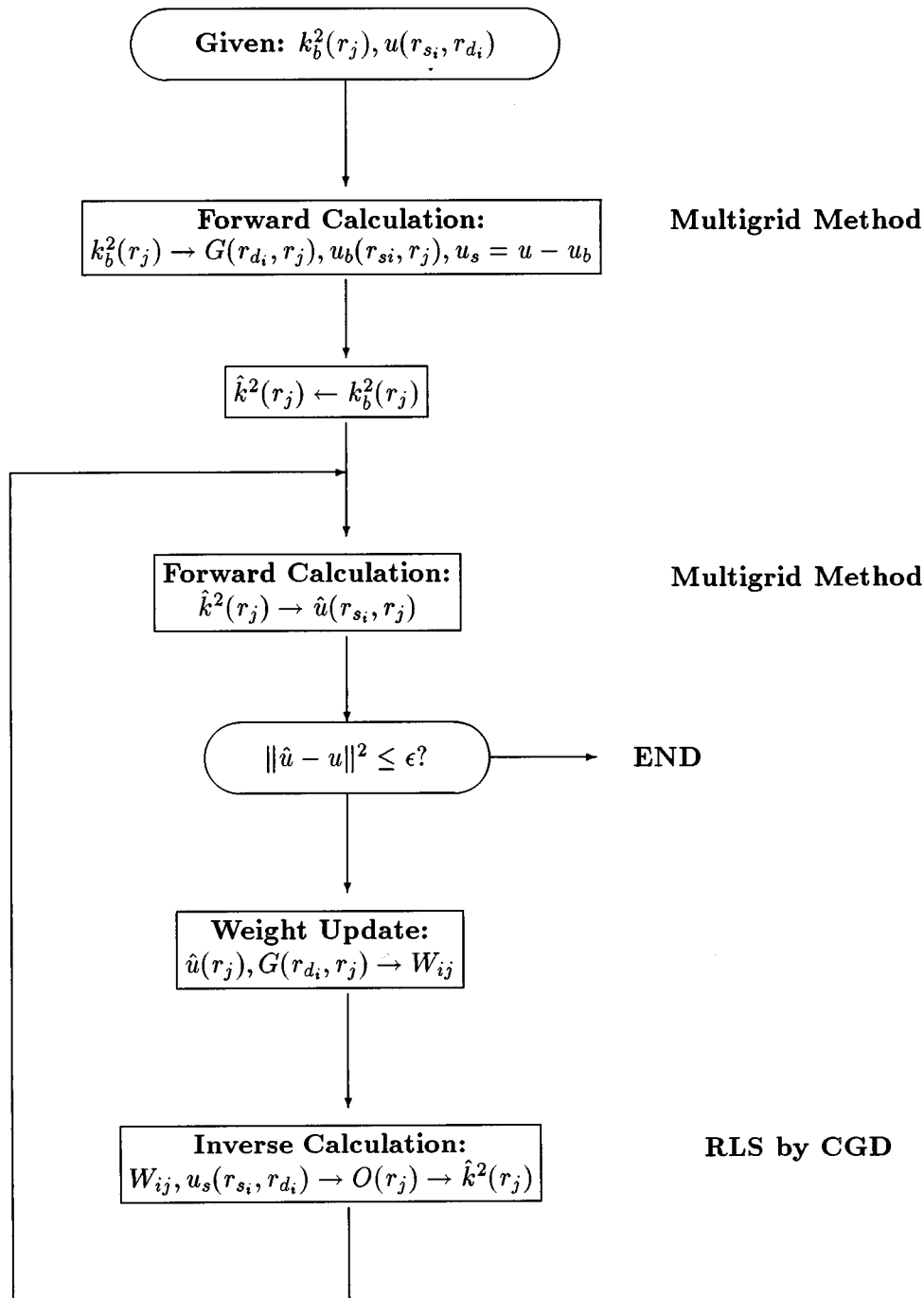
RLS by CGD

Fig. 3.   Flow chart of the BIM (RLS, regularized least-squares method; CGD, conjugate gradient descent).

is the residual on grid k. The solution of Eq. (6) at each grid level is solved by a relaxation sweep process given by the expression

$$u^k \leftarrow G^k(\tilde{u}^k, f^k), \qquad (11)$$

where $\tilde{u}^k$ is the initial solution used in the relaxation process, which is replaced by the new solution generated by G^k. The operator G^k represents the sweeps of a certain iterative process, such as the point Gauss–Seidel relaxation, the line Gauss–Seidel (in any combination of directions) relaxation, and the planar Gauss–Seidel (for 3D problems) relaxation.[26] The initial solution $\tilde{u}^k$ is normally generated by interpolation of the solution u^{k-1}, i.e., $\tilde{u}^k = I_{k-1}^k u^{k-1}$.

Figure 1 illustrates the basic idea of the full multigrid algorithm for a problem with $M = 4$ grid levels. The process starts on the coarsest grid $k = 1$, where the discrete approximation to Eq. (6) on this grid level u^1 is solved. The resulting solution is interpolated to the next finer grid, $k = 2$, to yield $\tilde{u}^2$ and is used as the first approximation to the solution u^2. The residual r^2 is then calculated, and the solution u^2 is obtained by a multigrid V cycle. We repeat this process, interpolating the solution from one level to the next as a first approximation and solving the residual by a V cycle, until the final solution is obtained on the finest level, $k = M$. In going from one level k to the next finer level, $k + 1$, the truncation error (which is due to discrete approximation of the actual continuous function) decreases by roughly the mesh element size ratio $(h_{k+1}/h_k)^p$, where h_k is the side length of an element at grid level k and p is the order of the difference approximation. The solution at each grid level by the full multigrid algorithm (shown by concentric circles in Fig. 1) is accurate to at least the level of the respective truncation error. Computational efficiency is gained because the final solution is achieved by evaluation of a series of problems having significantly fewer unknowns than would be required had the finest grid solution been computed directly. Hereafter we refer to this method as the MGFD method.

Validation of this method is illustrated in Fig. 2. Here we compare the amplitude and the phase values of the incident [Figs. 2(a) and 2(b)] and the scattered [Figs. 2(c) and 2(d)] fields, respectively, computed by the MGFD method and by an analytic method for an infinite 2D medium containing a circular object. The MGFD method is used to compute the solution in a 10 cm × 10 cm area with the object at the center. The Dirichlet boundary conditions were employed at the boundary of this area. The modulation frequency was 200 MHz. The optical properties of the background are $\mu_a{}^b = 0.05$ cm^{-1} and $\mu_s{}'^b = 20.0$ cm^{-1}. The object has a radius of 0.7 cm, and its optical properties are $\mu_a = 0.2$ cm^{-1} and $\mu_s{}' = 30.0$ cm^{-1}. A point source is located at a distance of 4 cm from the center of the object. The solution presented are for the incident and the scattering fields at the same distance, but at different angles with respect to the source. It can be seen that, in general, the accuracy of the amplitude and the phase increases with the mesh size from 33×33 ($h \simeq 3$ mm), 65×65 ($h \simeq 1.5$ mm) to 129×129 ($h \simeq 0.78$ mm). Results show very good agreement between the analytic solutions (a normal-mode se-
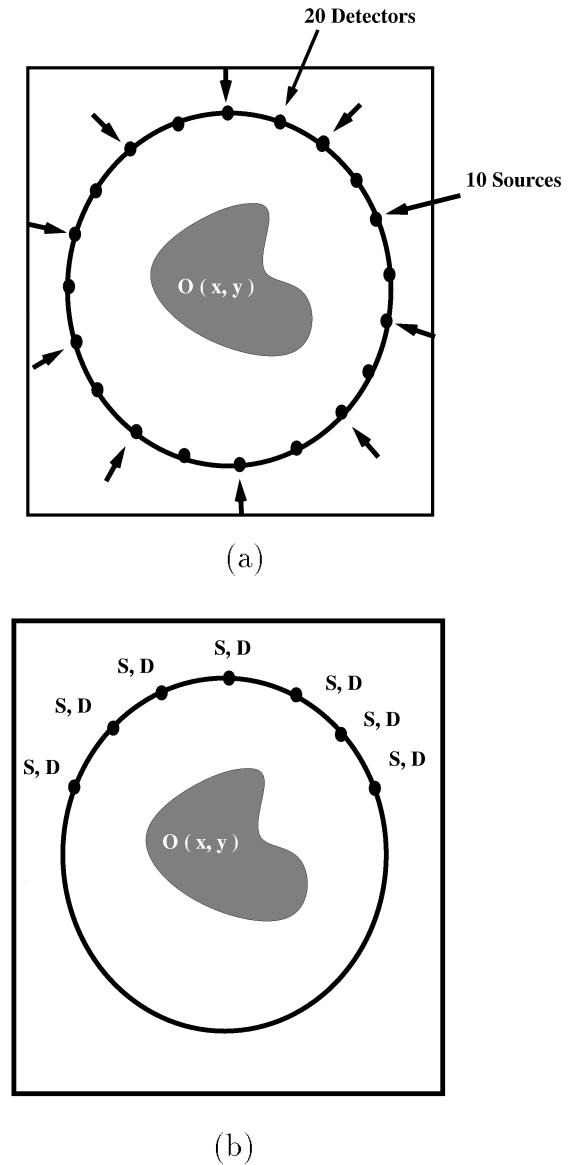

(a)

(b)

Fig. 4. (a) Data-acquisition geometry for full-angle profile inversion with 10 sources and 20 detectors in a uniform ring geometry. (b) Data-acquisition geometry for limited-angle profile inversion with 10 sources and 20 detectors distributed uniformly along a semicircle ranging from $-65°$ to $65°$. In both cases the radius of the source–detector ring is 4 cm. The object radius is 0.7 cm. The object is located either at the center or at an off-center location. $O(\mathbf{r})$ is the object function.

ries method[5] is employed to solve the Helmholtz equation in 2D cylindrical coordinates) and the numerical solutions at the finest grid level (129×129) for both the amplitude and the phase of the incident field and the amplitude of the scattering field. For the phase of the scattering field, the MGFD method fails to provide accurate results at locations opposite the source ($|\theta| > 100°$) with mesh size 129×129. A possible reason is that the absorption and the scattering perturbations are assigned as a step function in the simulated medium. There is a sharp discontinuity of the optical property at the boundary of the object, which may cause the error when the second term of the right-hand side of Eq. (2) is neglected.

Table 1. Medium Properties and Measurement Schemes in Different Simulation Studies

Test Case	Background Properties		Peak Perturbation		Object Location	ROI[a] Being Reconstructed
	μ_a (cm^{-1})	μ_s' (cm^{-1})	$\Delta\mu_a$ (cm^{-1})	$\Delta\mu_s'$ (cm^{-1})		
I Full angle	0.05	10.0	0.15	15.0	Center $a = 0$, $b = 0$	3.125 cm × 3.125 cm 40 × 40 elements
II Full angle	0.05	15.0	0.20	25.0	Off center $a = 1.5$, $b = 0$	3.125 cm × 3.125 cm 40 × 40 elements
III Full angle	0.05	15.0	0.20 0.15	15.0 20.0	Two objects $a_1 = 1.5$, $b_1 = 0$ $a_2 = -1.5$, $b_2 = 0$	6.25 cm × 3.59 cm 80 × 46 elements
IV Limited angle	0.05	15.0	0.20	15.0	Off center $a = 0$, $b = 1.5$	3.125 cm × 5.47 cm 40 × 70 elements

[a] ROI, region of interest.
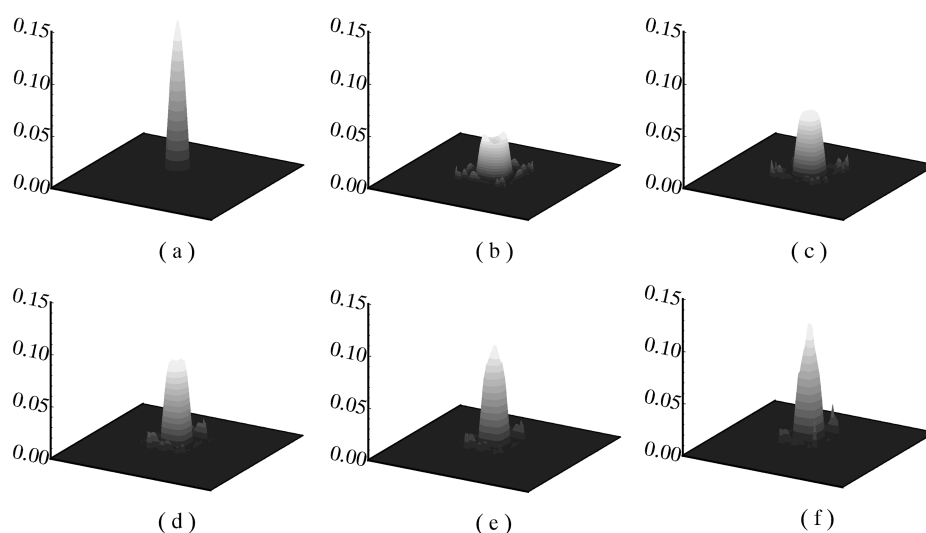
Fig. 5.   Reconstruction of the absorption coefficient for test case I: (a) image of the true perturbation; (b)–(f) reconstructed images after 1 (i.e., the Born approximation), 2, 3, 5, and 15 iterations, respectively.
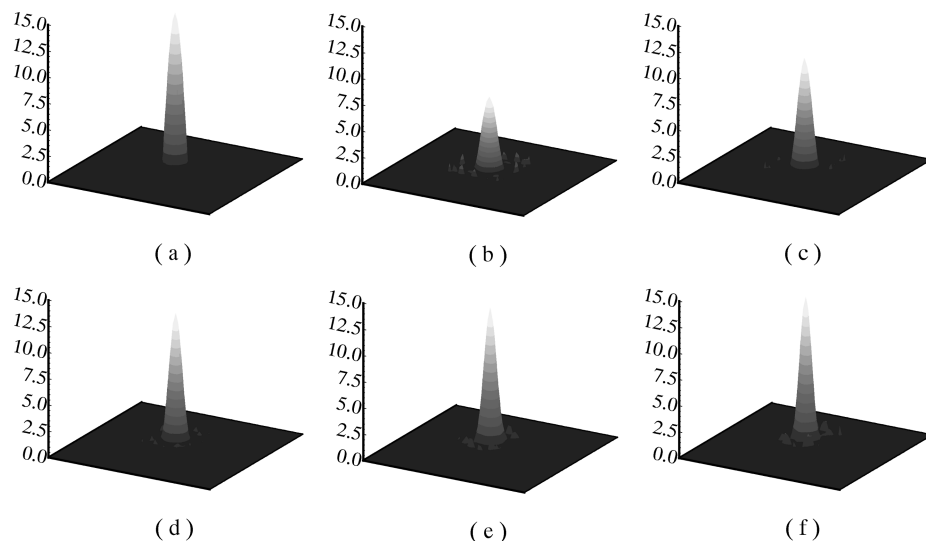

Fig. 6.   Reconstruction of the scattering coefficient for test case I: (a) image of the true perturbation; (b)–(f) reconstructed images after 1 (i.e., the Born approximation), 2, 3, 5, and 15 iterations, respectively.

The MGFD method employed in these studies is very efficient. A typical calculation with a mesh size of 129 × 129 takes approximately 45 s on a Sun SPARC 5 workstation.

3. INVERSE SOLUTION

A. Mathematical Model

Consider the test medium as a perturbation of a homogeneous background medium with absorption and scattering coefficients described by $\mu_a{}^b$ and $\mu_s{}'^b$, respectively, with an associated diffusion coefficient $D_b = [3(\mu_a{}^b + \mu_s{}'^b)]^{-1}$ and wave number $k_b{}^2 = -\mu_a{}^b/D_b + i\omega/cD_b$. Let $\mu_a = \mu_a{}^b + \delta\mu_a$, $\mu_s{}' = \mu_s{}'^b + \delta\mu_s{}'$, and define the object function as

$$O(\mathbf{r}) = k^2(\mathbf{r}) - k_b{}^2$$

$$= -3(\mu_a{}^b + \delta\mu_a)(\delta\mu_a + \delta\mu_s{}') - \frac{\delta\mu_a}{D_b}$$

$$+ i\,\frac{3\omega}{c}\,(\delta\mu_a + \delta\mu_s{}'), \tag{12}$$

which represents the unknown contrast between the object and the background medium. From Eq. (4), we can derive the following scalar wave equation:

$$\nabla^2 u(\mathbf{r}) + k_b{}^2 u(\mathbf{r}) = S(\mathbf{r}) - O(\mathbf{r})u(\mathbf{r}). \tag{13}$$

From Eq. (13) it can easily be shown that $u(\mathbf{r})$ satisfies the following nonlinear volume-integral equation:

$$\int_{\Omega} G(\mathbf{r}, \mathbf{r}')O(\mathbf{r}')u(\mathbf{r}')\mathrm{d}^2\mathbf{r}' = u(\mathbf{r}) - u_b(\mathbf{r}), \tag{14}$$

where $u_b(\mathbf{r})$ is the background field (i.e., the total field of the background medium under the same source illumination) and $G(\mathbf{r}, \mathbf{r}')$ is the Green's function of the homogeneous background that satisfies

$$\nabla^2 G(\mathbf{r}, \mathbf{r}') + k_b{}^2 G(\mathbf{r}, \mathbf{r}') = -\delta(\mathbf{r} - \mathbf{r}'). \tag{15}$$

In this paper we refer to

$$u_s(\mathbf{r}) = u(\mathbf{r}) - u_b(\mathbf{r}) \tag{16}$$

as the scattering field. We assume that the background field is known either from experiment or by numerical solution, so that the scattering field can be derived from the measured total field and the background field.

B. Born Iterative Method for Image Reconstruction

In the previous sections, we have used $u(\mathbf{r})$, $u_b(\mathbf{r})$, and $u_s(\mathbf{r})$ to represent the total, the background, and the scattering fields at $\mathbf{r}$, respectively, that are due to a point source located at $\mathbf{r_s}$. In optical imaging, multiple sources and detectors are often used. To express explicitly the dependence of these fields on the source locations, hereafter we use $u(\mathbf{r}, \mathbf{r}_s)$, $u_b(\mathbf{r}, \mathbf{r}_s)$, and $u_s(\mathbf{r}, \mathbf{r}_s)$ to denote these three functions, respectively. The integral equation (14) can be discretized to yield a complex linear system of equations as follows:

$$\mathbf{W}_{(m \times n)}\mathbf{O}_{(n \times 1)} = \mathbf{u}_{s_{(m \times 1)}} \tag{17}$$

where $\mathbf{O} = [O(\mathbf{r}_j), \; j = 1, 2, \ldots, n]^T$ is composed of the values of $O(\mathbf{r})$ at various voxels $\mathbf{r}_j$; $\mathbf{u} = [u_s(\mathbf{r}_{d_i}, \mathbf{r}_{s_i}), \; i$
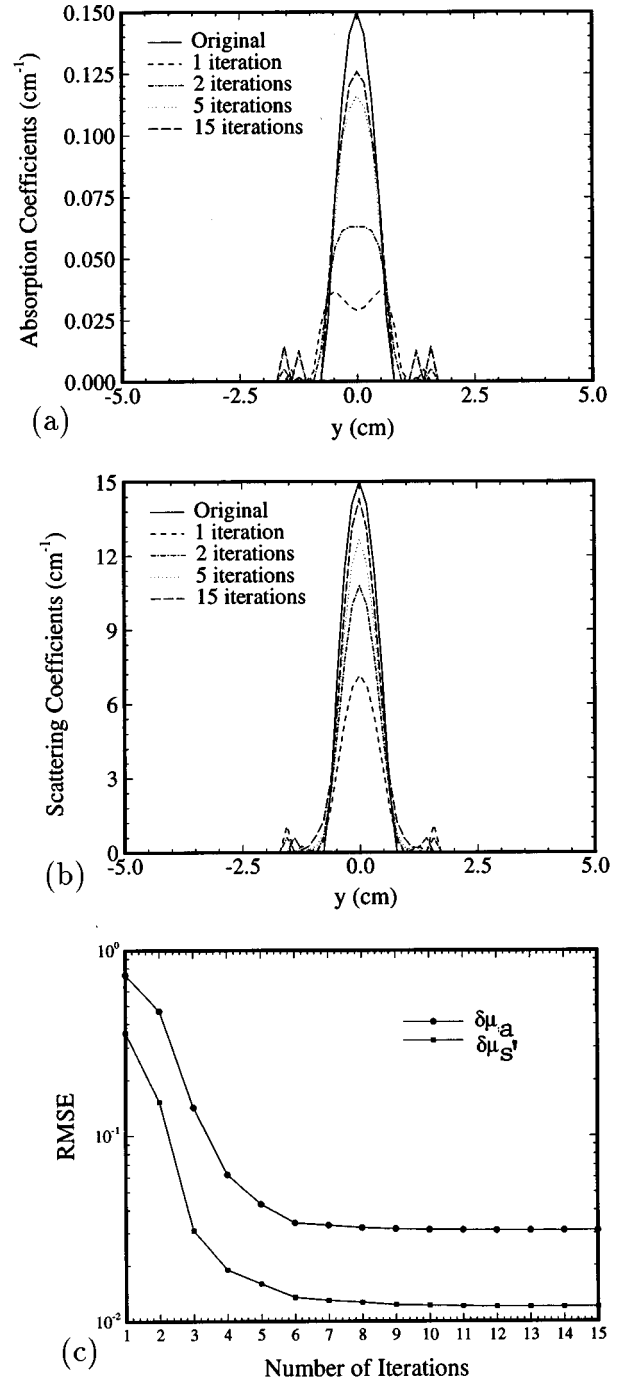

Fig. 7. Cross-sectional cuts along the y axis passing through the object center for (a) the absorption reconstruction shown in Fig. 5 and (b) the scattering reconstruction shown in Fig. 6. (c) Relative RMSE's of the reconstructed absorption distribution (circles) and the scattering distribution (squares) as functions of iteration steps.

$= 1, 2, \ldots, m]^T$ consists of the scattered field obtained with different source–detector pairs $(\mathbf{r}_{d_i}, \mathbf{r}_{s_i})$; and $\mathbf{W}$ is a weight matrix with elements

$$W_{ij} = G(\mathbf{r}_{d_i}, \mathbf{r}_j)u(\mathbf{r}_j, \mathbf{r}_{si})\delta v \qquad i = 1, \ldots, m,$$

$$j = 1, \ldots, n, \tag{18}$$

where δv is the volume of a voxel. The coefficients of the weight matrix depend on the total field and on the Green's function. Since the total field depends on the unknown object function, this is a nonlinear equation. To solve Eq. (17), we adopt the following iterative method.

Given the measured total field $u(\mathbf{r}_d, \mathbf{r}_s)$ and the background medium $k_b{}^2(\mathbf{r})$:

1. Solve the Green's function $G(\,,\,)$ and the background field $u_b(\,,\,)$, based on $k_b{}^2(\,)$, using the MGFD method. Set $u_s(\mathbf{r}_d, \mathbf{r}_s) = u(\mathbf{r}_d, \mathbf{r}_s) - u_b(\mathbf{r}_d, \mathbf{r}_s)$.
2. Let $\hat{u}(\mathbf{r}, \mathbf{r}_s) = u_b(\mathbf{r}, \mathbf{r}_s)$, i.e., the Born approximation.
3. Calculate the weight matrix **W** from the previously calculated total field $\hat{u}(\,,\,)$ and the Green's function $G(\,,\,)$, according to Eq. (18).
4. Solve the perturbation equation given in Eq. (17) for the object function $O(\mathbf{r})$ by employing the Tikhonov

regularization optimization process, using the conjugate gradient descent method.[27,28] Here, because the perturbation equation is complex, the conjugate gradient descent method in Ref. 28 has been extended to handle complex variables.

5. Using the recently found $O(\mathbf{r})$ and hence the new estimate of $k^2(\mathbf{r})$, solve the total field $\hat{u}(\mathbf{r}, \mathbf{r}_s)$ by the MGFD method.
6. Compare the measured total field $u(\mathbf{r}, \mathbf{r}_s)$ with the total field $\hat{u}(\mathbf{r}, \mathbf{r}_s)$ obtained in step 5. If the two quantities are within an acceptable value, stop the iterations. Otherwise, go back to step 3.

Figure 3 is a flow chart of this algorithm.

C. Simultaneous Reconstruction of Absorption and Scattering Distributions

With frequency-domain data, the object function $O(\mathbf{r})$ is a complex function of absorption and scattering distribu-
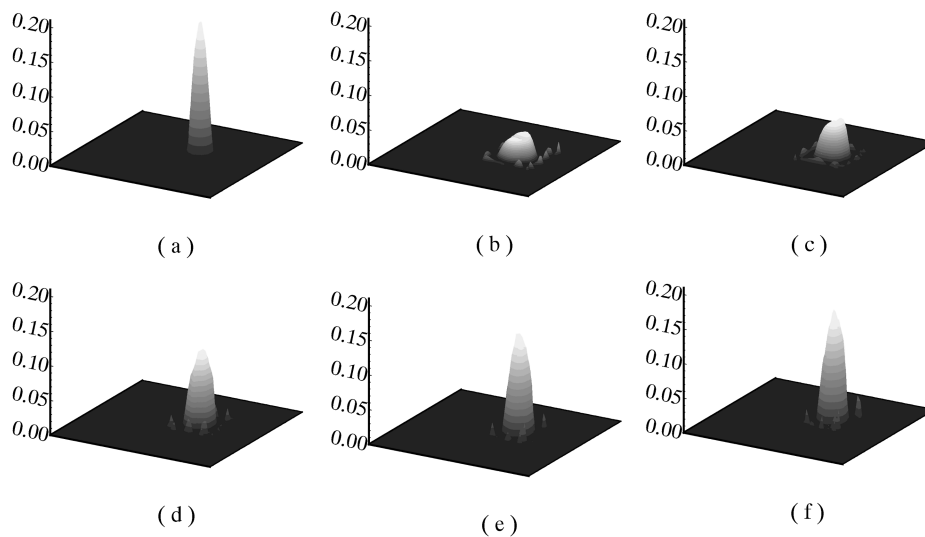

Fig. 8. Reconstruction of the absorption coefficient for test case II: (a) image of the true perturbation; (b)–(f) reconstructed images after 1, 2, 5, 8, and 15 iterations, respectively.
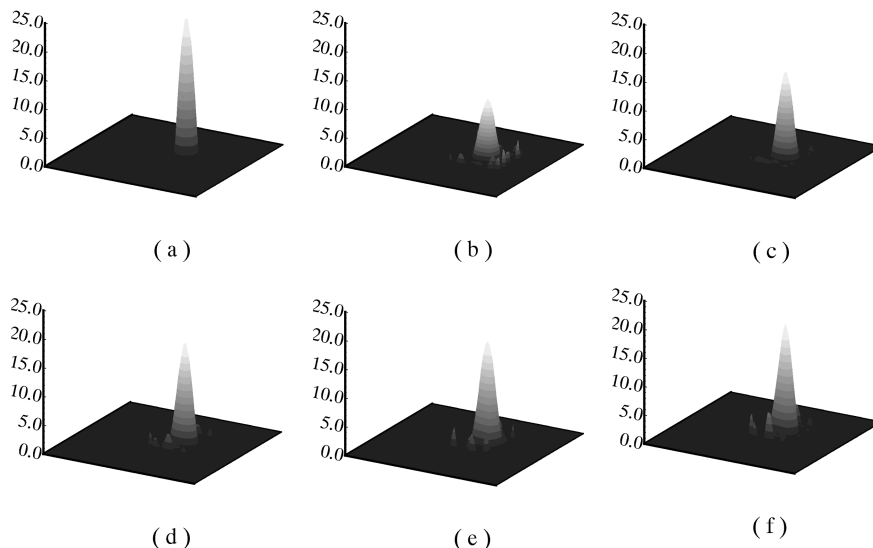

Fig. 9. Reconstruction of the scattering coefficient for test case II: (a) image of the true perturbation; (b)–(f) reconstructed images after 1, 2, 5, 10, and 15 iterations, respectively.
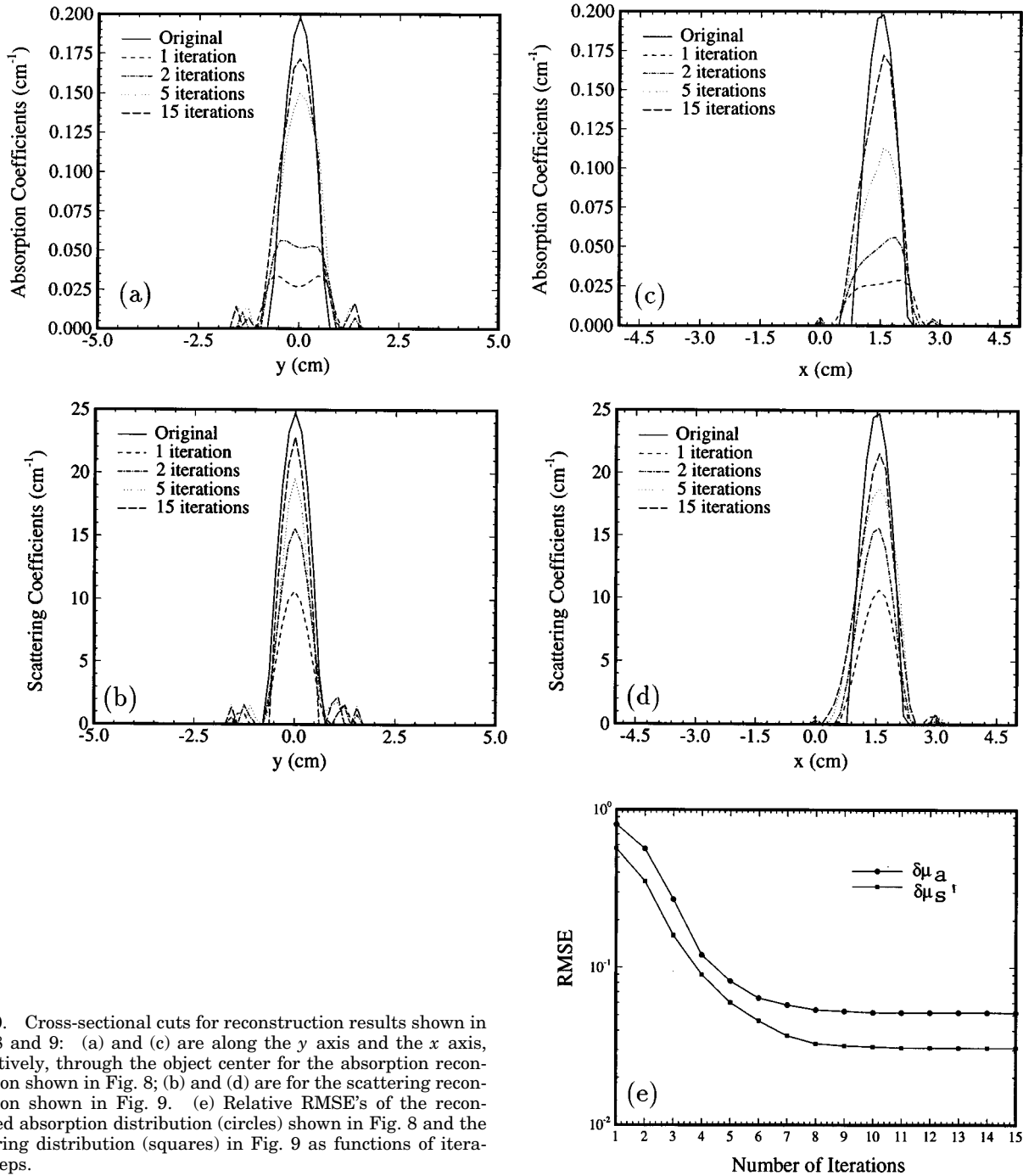
Fig. 10. Cross-sectional cuts for reconstruction results shown in Figs. 8 and 9: (a) and (c) are along the y axis and the x axis, respectively, through the object center for the absorption reconstruction shown in Fig. 8; (b) and (d) are for the scattering reconstruction shown in Fig. 9. (e) Relative RMSE's of the reconstructed absorption distribution (circles) shown in Fig. 8 and the scattering distribution (squares) in Fig. 9 as functions of iteration steps.

tions. We can find the absorption and the scattering coefficients from the real part and the imaginary part of the object function. From Eq. (12) we obtain

$$Re[O(\mathbf{r})] = -3(\mu_a^b + \delta\mu_a)(\delta\mu_a + \delta\mu_s') - [(\delta\mu_a)/D_b], \tag{19}$$

$$Im[O(\mathbf{r})] = [(3\omega)/c](\delta\mu_a + \delta\mu_s'). \tag{20}$$

Solving the above two equations, we obtain the absorption and the scattering coefficients as follows:

$$\delta\mu_a(\mathbf{r}) = -\frac{\mu_a^b \dfrac{Im[O(\mathbf{r})]}{\omega/c} + Re[O(\mathbf{r})]}{\dfrac{Im[O(\mathbf{r})]}{\omega/c} + 3(\mu_a^b + \mu_s'^b)}, \tag{21}$$

$$\delta\mu_s'(\mathbf{r})$$

$$= \frac{\left\{ Re[O(\mathbf{r})] + 3(3\mu_a^b + \mu_s'^b) + \dfrac{Im[O(\mathbf{r})]}{\omega/c} \right\} \dfrac{Im[O(\mathbf{r})]}{3\omega/c}}{\dfrac{Im[O(\mathbf{r})]}{\omega/c} + 3(\mu_a^b + \mu_s'^b)}. \tag{22}$$

From Eqs. (21) and (22) the perturbations in absorption and scattering distributions can easily be derived once the complex object function (i.e., the perturbation in the wave number) is obtained.

4. RESULTS

Figure 4 illustrates the acquisition geometry employed. Within a 10 cm $\times$ 10 cm square are situated 10 sources and 20 detectors deployed either in a uniform ring geometry [Fig. 4(a)] or in a more restricted fashion about the center [Fig. 4(b)]. The latter were spaced uniformly along a semicircle ranging from $-65°$ to $65°$ in a reflectance mode. For both geometries the radius of the source–detector ring is 4 cm. The source modulation frequency used is 200 MHz. In all cases, the radius of the added object is $R = 0.7$ cm, and the absorption and scat-

tering perturbations follow a sinusoidal distribution defined by $\delta\mu(x, y) = \Delta\mu \cos\{\pi/2R[(x - a)^2 + (y - b)^2]^{1/2}\}$, where $\Delta\mu$ represents the peak perturbation in absorption or scattering coefficient and the values for a and b indicate object locations. The sinusoidal distribution is used to simulate gradual changes normally associated with a tumor. Table 1 lists the medium properties and measurement schemes used in four test media. Note that the contrast in the absorption and the scattering coefficient of the object is up to 4 and 2.5 times the background, respectively. To obtain the forward and the inverse solutions, the test medium is discretized to 128×128 square elements ($h = 10/128 = 0.078125$ cm) with 129×129 grid points. The forward solution was obtained by the MGFD method, with the finest grid size being 129×129. For the inverse solution, to save computation time, we solved only a subregion in the medium
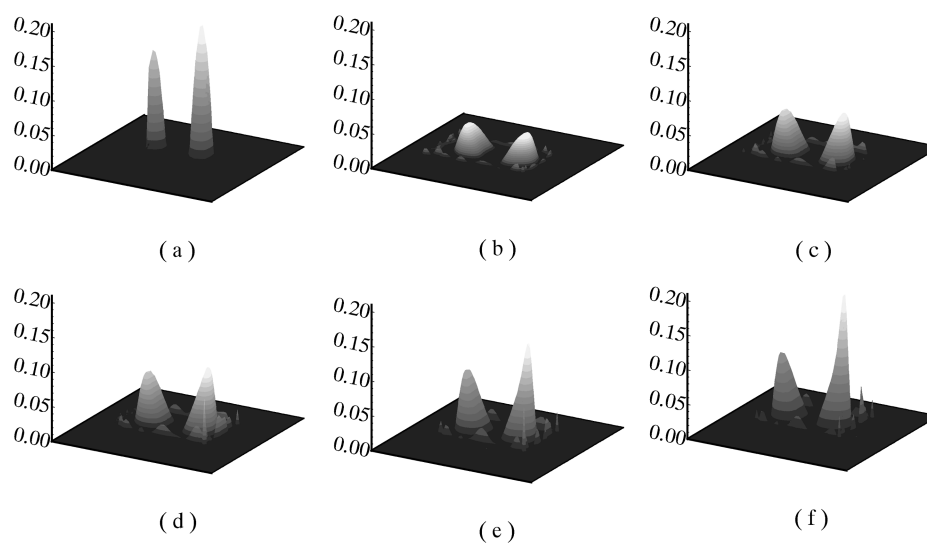

Fig. 11.   Reconstruction of the absorption distribution for test case III: (a) image of the true perturbation; (b)–(f) reconstructed images after 1, 2, 3, 5, and 15 iterations, respectively.
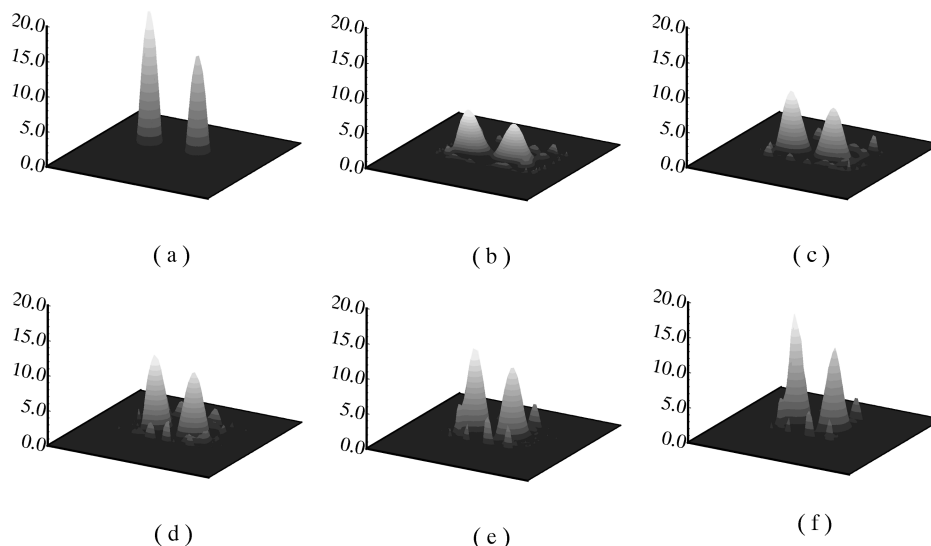

Fig. 12.   Reconstruction of the scattering distributions for test case III: (a) image of the true perturbation; (b)–(f) reconstructed images after 1, 2, 5, 10, and 15 iterations, respectively.

that contains the object. This is accomplished based on the assumption that with a preprocessing step, a region of interest (ROI) can be identified. One possible way is to use the Born approximation to reconstruct the entire medium, from which we can identify a ROI. The size and the location of the ROI for each test case are also listed in Table 1.

To compare the overall accuracy of the reconstructions, we introduce the relative root-mean-square error (RMSE) of the reconstructed profile as a function of the iteration steps. The relative RMSE is defined as

$$\text{RMSE}^{(i)} = \left\{ \frac{\Sigma_j [\alpha_j^{(i)} - \alpha_j]^2}{\Sigma_j (\alpha_j)^2} \right\}^{1/2}, \qquad (23)$$

where $\alpha_j^{(i)}$ is the reconstructed value of the absorption or the scattering coefficients in the ith iteration and in the jth cell, with α_j being the actual value. The summation is calculated over the ROI for each test medium.

A. Full-Angle Profile Inversion Without Noise

1. Test Media I: a Centered Rod
Figures 5 and 6 show a 3D plot of the spatial distribution of the value of the absorption and the scattering coefficients, respectively, of the object and those of the reconstructed profiles after the indicated number of iterations. The target profile is shown in Figs. 5(a) and 6(a). Figures 5(b) and 6(b) show the results with the first-order Born approximation. The results with subsequent 2, 3, 5, and 15 iterations are shown in Figs. 5(b)–5(f) and 6(b)–6(f). It can be seen that the reconstruction result after 15 iterations [see Figs. 5(f) and 6(f)] is quite accurate, with significant improvement in terms of both spatial range and perturbation intensities, compared with the result obtained with 1 iteration. Actually, the result obtained after 8 iterations is almost identical to the one obtained after 15 iterations. Cross-sectional cuts through the center of the object along the y axis for the target and reconstructions are shown in Figs. 7(a) and 7(b). Interestingly, we observe that the reconstructed scattering coefficient is closer to the true value than is the absorption coefficient.

Figure 7(c) shows the relative RMSE of the reconstructed absorption and scattering distributions in Figs. 5 and 6 as a function of the iteration steps. Under the following convergence criterion:

$$\left| \frac{\text{RMSE}^{(i+1)} - \text{RMSE}^{(i)}}{\text{RMSE}^{(i)}} \right| < 10^{-6}, \qquad (24)$$

the convergence is reached after approximately 11 and 12 iterations for the absorption and the scattering reconstructions, respectively.

2. Test Media II: an Off-Center Rod
Figures 8 and 9 show results similar to those shown in Figs. 5 and 6, but for an object located 1.5 cm from the center. The target profile is shown in Figs. 8(a) and 9(a). As in the case for the centrally located object, location of the object is accurately determined for both coefficients after only one iteration [Figs. 8(b) and 9(b)], but edge broadening is evident. With additional iterations, shown in Figs. 8(c)–8(f) and 9(c)–9(f), significant improvements
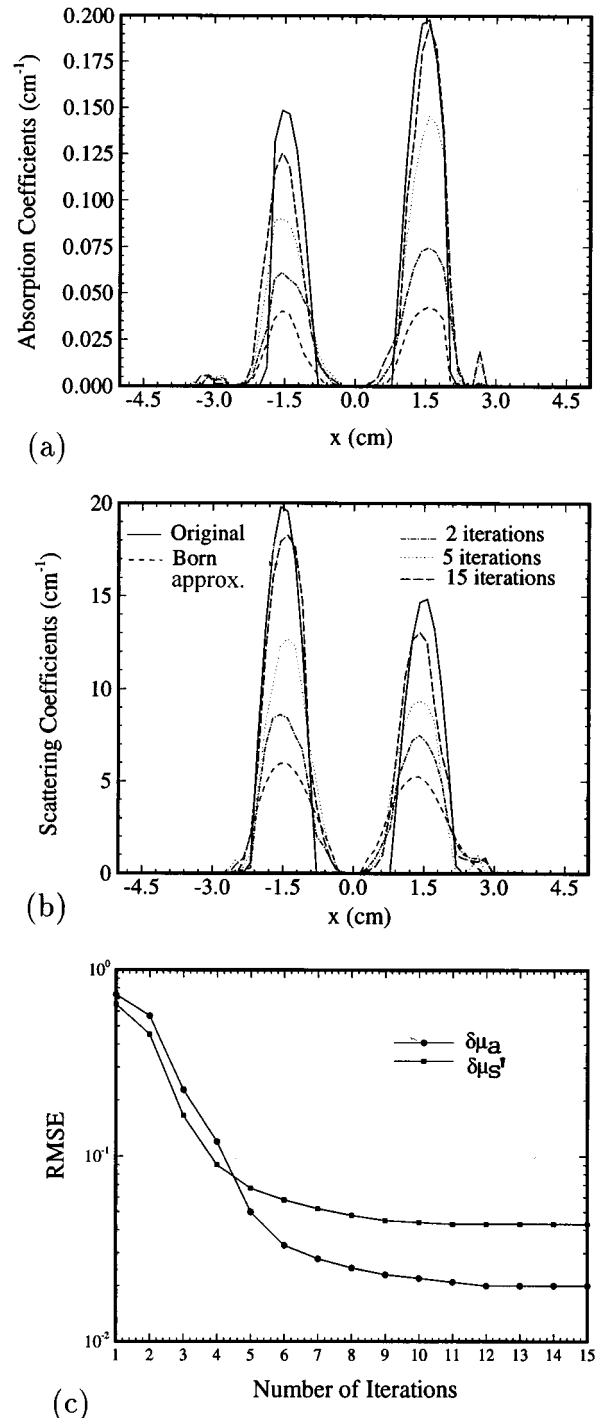

(a)

(b)

(c)

Fig. 13. Cross-sectional cuts along the x axis passing through the centers of the two objects for (a) the absorption reconstruction shown in Fig. 11 and (b) the scattering reconstruction shown in Fig. 12. (c) Relative RMSE's of the reconstructed absorption distribution (circles) in Fig. 11 and the scattering distribution (squares) shown in Fig. 12 as functions of iteration steps.

are achieved, although some artifact in the vicinity of the object is present. These improvements are apparent in the cross-sectional cuts through the center of the object along the two main axes, as shown in Figs. 10(a)–10(d).

Figure 10(e) shows the RMSE values of the reconstructed absorption and scattering distributions in Figs. 8
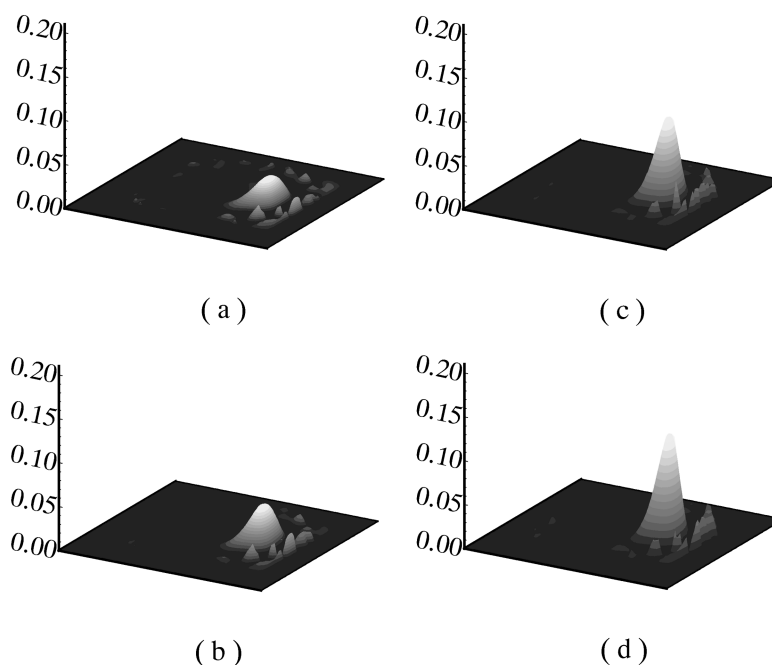
Fig. 14.   Reconstruction of the absorption distributions from noisy data with a SNR of 25 dB.   (a)–(d) Reconstructed images after 1, 2, 5, and 15 iterations, respectively.   The target medium is shown in Fig. 8(a).
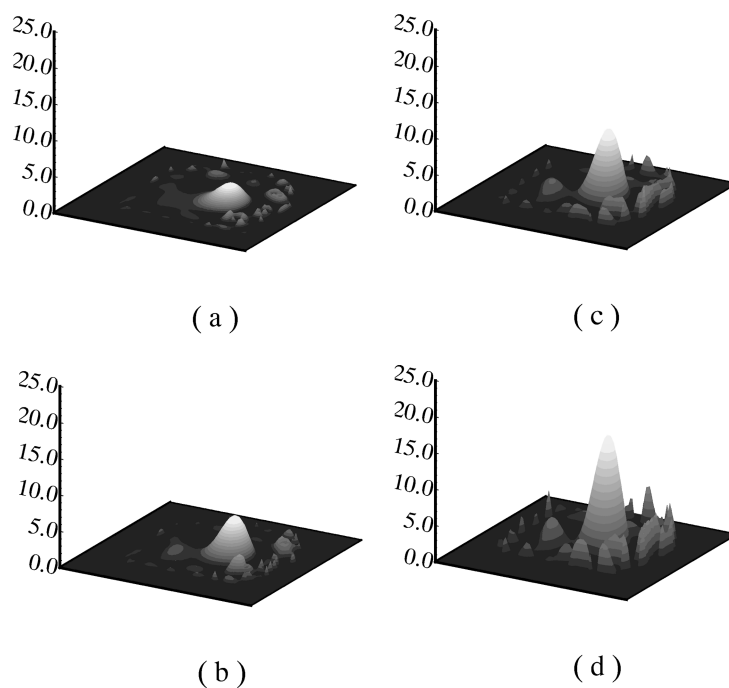

Fig. 15.   Reconstruction of the scattering distributions from noisy data with a SNR of 25 dB.   (a)–(d) Reconstructed images after 1, 2, 5, and 15 iterations, respectively.   The target medium is shown in Fig. 9(a).

and 9 as a function of the iteration number.   By means of the same convergence criterion as before, convergence is reached for absorption and scattering reconstructions after approximately 10 and 11 iterations, respectively.

3.   Test Case III: Two Separated Rods
Figures 11 and 12 show results for a medium containing two objects having a radius of 0.7 cm, separated by 3 cm

and located equidistant from the center.   The target profile is shown in Figs. 11(a) and 12(a).   Qualitatively, the results obtained are similar to the cases with one object. The objects are accurately located after the first iteration, as shown in Figs. 11(b) and 12(b), but edge broadening and artifacts are present.   On subsequent iterations, significant quantitative improvements are achieved.   Figures 13(a) and 13(b) show the reconstructed absorption

and scattering distributions along the x axis passing through the center of the two objects.

In Fig. 13(c) we show the relative RMSE values, from which we can see that the convergence is reached after 13 and 12 iterations for the absorption and the scattering reconstructions, respectively.

B. Full-Angle Profile Inversion with Noise

To evaluate the effect of noise on the stability of the algorithm, random noise with a Gaussian distribution is added to the real part and the imaginary part of the scattering field. The noise level is measured by the SNR, defined as
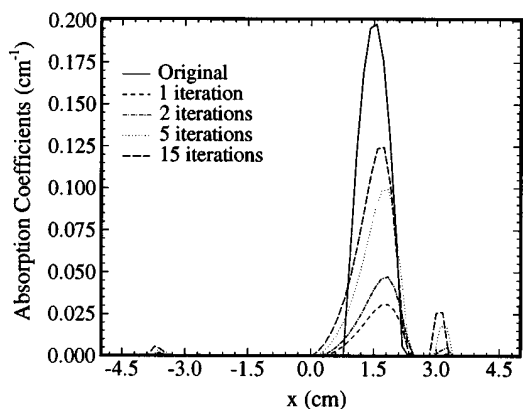
$$\text{SNR} = 10 \log \frac{P_u}{P_N}, \qquad (25)$$

where P_u is the power of the scattering field and P_N is the noise power.
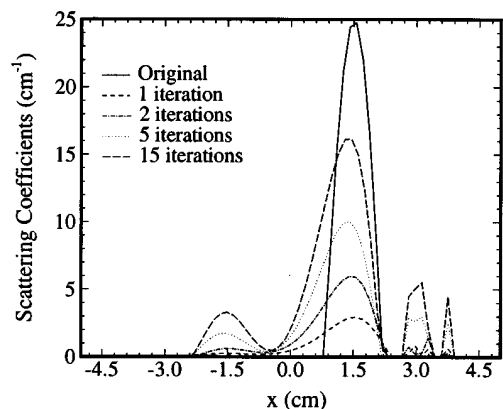
1. Test Case II: an Off-Center Rod

Figures 14 and 15 show the reconstructions of absorption and scattering distributions from noise-added data with a SNR of 25 dB (i.e., 5.6% noise) for the same case as used in Figs. 8 and 9, except the ROI becomes 6.4 cm $\times$ 6.4 cm. Compared with the case without noise (Figs. 8 and 9), the reconstruction profiles are blurred, although the results after 15 iterations are still quite accurate. Figures 16(a) and 16(b) show the reconstructed absorption and scattering distributions along the x axis passing through the center of the object.

We also attempted reconstruction in the presence of stronger noise. We found that the algorithm starts to break down at a SNR of approximately 20 dB.

Fig. 16. Cross-sectional cuts along the x axis passing through the centers of the object for (a) the absorption reconstruction shown in Fig. 14 and (b) the scattering reconstruction shown in Fig. 15.
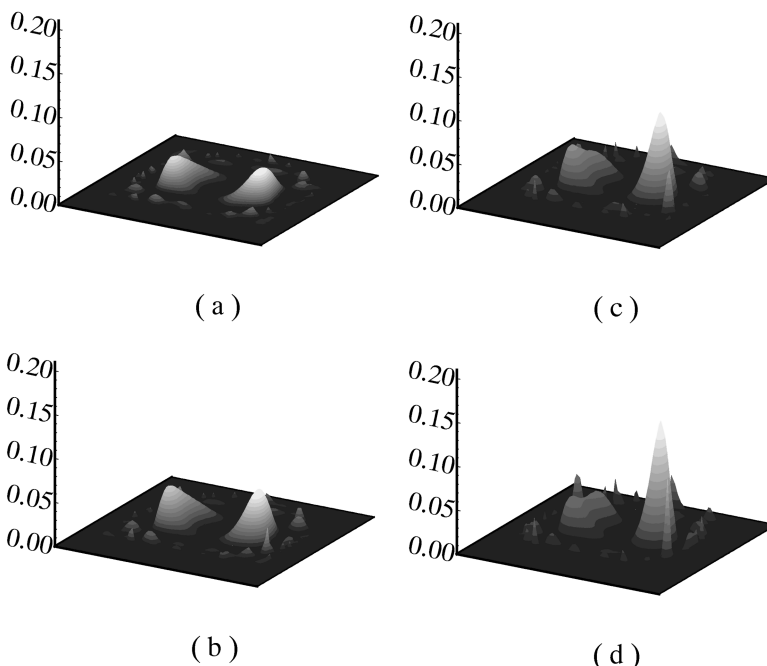
Fig. 17. Reconstruction of the absorption distributions from noisy data with a SNR of 25 dB. (a)–(d) Reconstructed images after 1, 2, 5, and 15 iterations, respectively. The target medium is shown in Fig. 11(a).
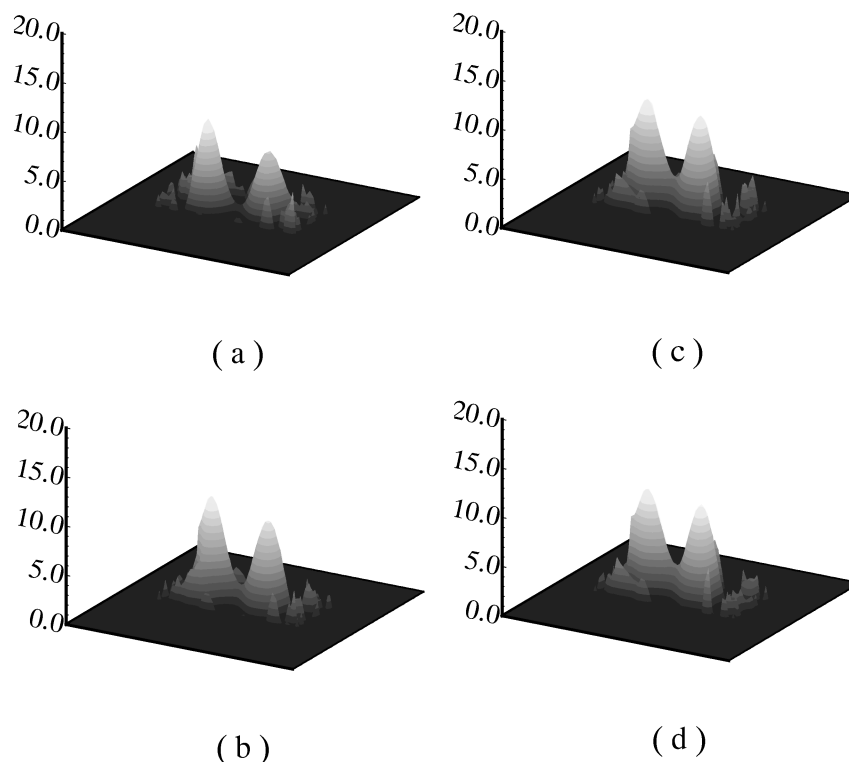
Fig. 18. Reconstruction of the scattering distributions from noisy data with a SNR of 25 dB.   (a)–(d) Reconstructed images after 1, 2, 5, and 15 iterations, respectively.   The target medium is shown in Fig. 12(a).
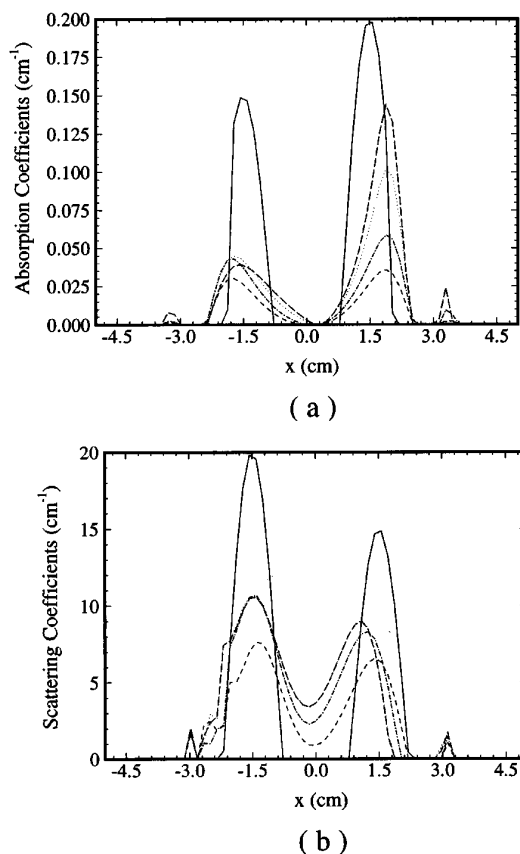

Fig. 19.   Cross-sectional cuts along the x axis passing through the centers of the two objects for (a) the absorption reconstruction shown in Fig. 17 and (b) the scattering reconstruction shown in Fig. 18.

2. Test Case III: Two Separated Rods

Figures 17 and 18 show the reconstructions of absorption and scattering distributions from noise-added data with a SNR of 25 dB for the same medium as was used for Figs. 11 and 12, except the ROI becomes 7.6 cm × 7.6 cm.   The cross-sectional cuts are shown in Figs. 19(a) and 19(b).   It can be seen that the locations of two reconstructed objects are slightly shifted from actual positions.   An interesting phenomenon, shown in Fig. 17, is that, whereas the reconstructed absorption values of one object improves continuously on successive iterations, that of the other object remains the same after 2 iterations.   For scattering reconstructions, shown in Fig. 18, the peak values of the final reconstruction after 15 iterations (actually the value stays the same after 5 iterations) are approximately half of the true profile [see Fig. 18(b)].

C. Limited-Angle Profile Inversion without Noise

1. Test Case IV: an Off-Center Rod

It is appreciated that the full-angle measurement schemes used in the previous examples may not always be feasible in practice.   Here we consider the limited-angle measurement scheme shown in Fig. 4(b).   Figures 20 and 21 show the target and the reconstruction profiles of the computed absorption and scattering distributions after the indicated number of iterations for an off-center object with a limited-angle illumination.   Cross-sectional cuts through the center of the object are shown in Figs. 22(a) and 22(b).   It can be seen that, when the measurement is performed over a limited view, the reconstruction quality is still quite satisfactory.
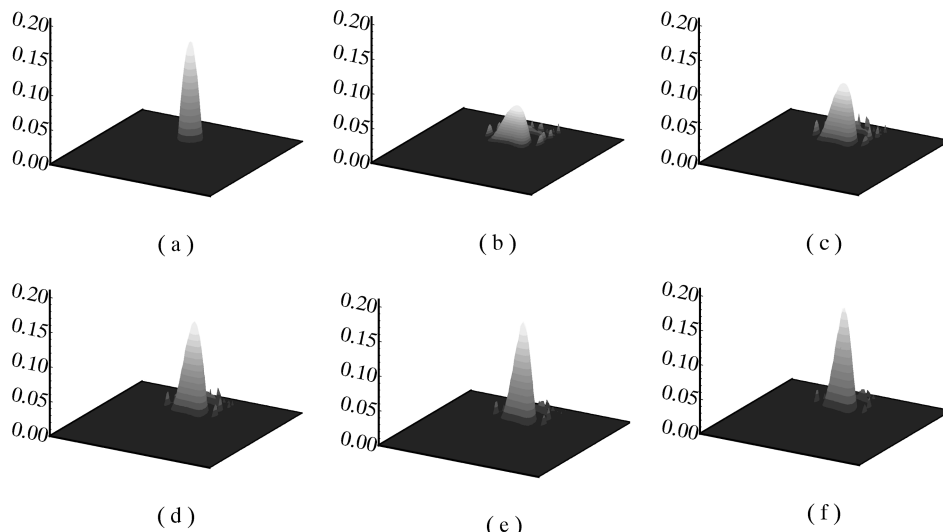
Fig. 20. Limited-angle reconstruction of the absorption coefficient for test case IV: (a) image of the true perturbation; (b)–(f) reconstructed images after 1, 2, 5, 8, and 15 iterations, respectively.

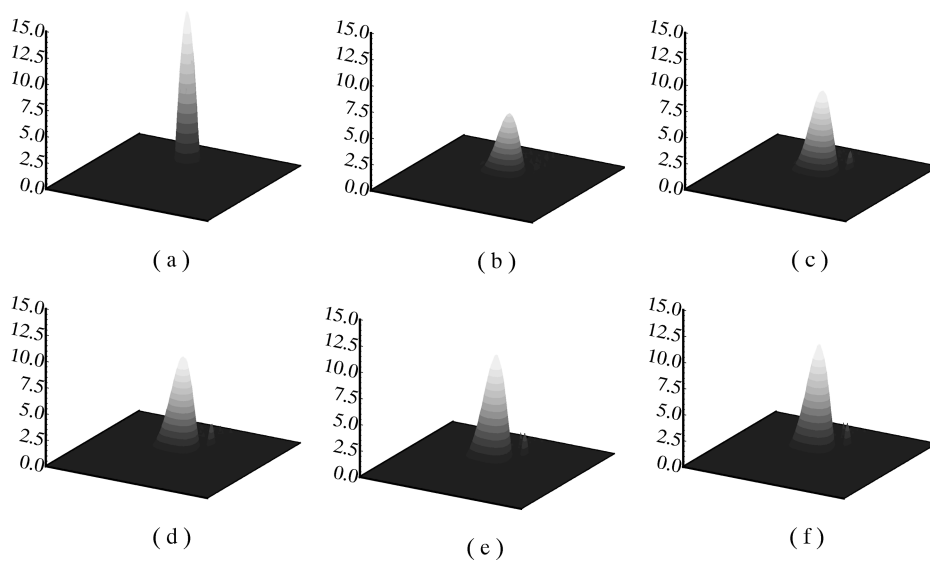Fig. 21. Limited-angle reconstruction of the scattering coefficient for test case IV: (a) image of the true perturbation; (b)–(f) reconstructed images after 1, 2, 5, 10, and 15 iterations, respectively.
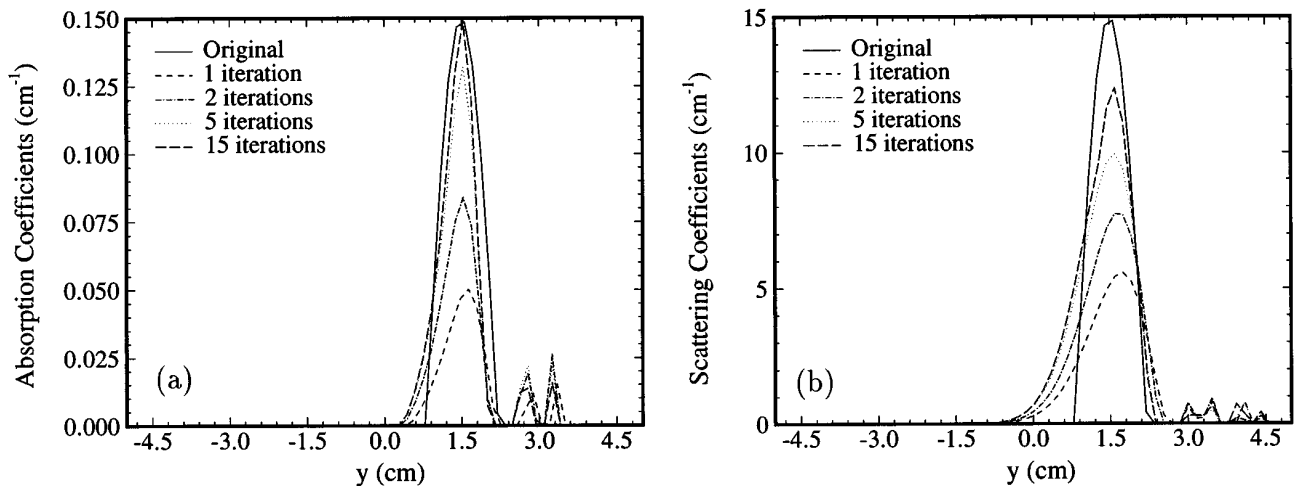

Fig. 22. Cross-sectional cuts along the y axis passing through the object center for (a) the absorption reconstruction shown in Fig. 20 and (b) the scattering reconstruction shown in Fig. 21.

5. SUMMARY AND DISCUSSION

In summary, we have evaluated a Born iterative method (BIM) for the simultaneous reconstruction of absorption and scattering distributions of added objects to otherwise homogeneous turbid media by means of frequency-domain data. The approach is based on iterative solutions of a linear perturbation equation, which is derived from the integral form of Helmholtz wave equation for photon-density waves. This equation is a good approximation of the diffusion equation when the optical properties of the medium change smoothly. In each iteration the total field and the object function are updated. The object function represents the perturbation in the complex wave number. A multigrid finite difference (MGFD) method is used to calculate the forward solution (the total field). A regularized least-squares method is used to solve the inverse problem (the object function). The absorption and the scattering coefficients are obtained from the complex object function. This method has been applied to several test media containing one or two objects with strong but smoothly varying perturbation from the background properties. Reconstructions from full-angle as well as limited-angle data (obtained by the MGFD method) have been attempted. From the reconstruction results, we conclude that the algorithm can yield quantitatively (in terms of coefficient values) and qualitatively (in terms of location and shape) accurate reconstructions for both absorption and scattering coefficients and that it is computationally efficient. The algorithm is also quite robust to noise in data.

Recognizing that limitations in available views occur often in practical measurements, we have determined the accuracy and the quality of reconstructed images under these conditions. When restricted to a view angle mostly in a reflectance geometry, we observed some loss of edge resolution for the side of the object opposite the sources. This finding is encouraging, particularly as it may relate to possible applications intended for imaging of pathologies (e.g., hematomas) in an adult brain, in which transmission measurements likely are not practical.

The first iteration of the BIM reported here is equivalent to the Born approximation. O'Leary *et al.*[12] have shown that the Rytov approximation produced more-accurate reconstructions of the absorption coefficient than did the Born approximation. However, they observed that, overall, the recovered coefficients were significantly lower than the true values, especially as the strength of the perturbation is increased. We observed qualitatively similar results for the Born approximation but showed that, with successive iterations, quantitatively accurate recovery is possible for both absorption and scattering coefficients.

In the reported simulation results, one obtains the data by solving the wave equation numerically, which is an approximation to the diffusion equation. The approximation is valid in the test media simulated here, where the optical properties change smoothly in a sinusoidal pattern. To generate more realistic data, one could solve the diffusion equation directly, using the MGFD method or a finite element method. Reconstruction accuracies ob-

tained from these data should be evaluated to validate the usefulness of the proposed scheme. Of course, ultimately, validation with real measurement data are required.

Since the original reports in the early 1990's,[14,29–31] interest in the problem of optical tomographic imaging in highly scattering media and its applications to near-infrared imaging of tissue have increased greatly. Many of the reports on the imaging problem have been qualitative in nature, with the primary aim being to demonstrate that recognizable images of simple objects embedded in otherwise homogeneous media can be computed.[32] Nearly all the inverse schemes described employ iterative perturbation approaches.[7,13] These schemes are first described for the recovery of either absorption or scattering coefficient. Recently, these have been expanded to consider the simultaneous recovery of both absorption and scattering coefficients.[10,12,21,33] Comparison of results in this report with those of others is difficult because of the lack of details regarding the number of iterations employed and because of the absence of an objective measure of image quality. Here we have adopted as an objective measure the relative root-mean-square error, which is commonly used in other imaging modalities. Using this measure under the conditions examined, we have demonstrated accurate quantitative recovery of the optical coefficients and their location. We consider this finding encouraging but recognize that further evaluation under more realistic conditions is needed. Because an objective measure of image quality is lacking from most reports in this field, we recommend that the method described here be adopted. This will be especially important for efforts to compare results obtained from different data collection and analysis schemes.

A major difference between the scheme described here and the iterative perturbation approaches described previously in Refs. 7, 9, and 13 is that our perturbation equation is derived from the integral form of the wave equation, whereas others used the first-order Taylor approximation. In both cases the elements in the weight matrix consist of the product of the incident field and the Green's function. In the BIM reported here, only the incident field needs to be updated. We have also investigated the use of the DBIM, which updates both the incident field and the Green's function.[34] Note that the perturbation approaches derived based on the Taylor approximation are essentially similar to the DBIM. For the microwave imaging problem, both Wang and Chew[15,16] have shown that the DBIM converges faster than the BIM, but that the BIM is less sensitive to noise. This phenomenon has also been observed in our preliminary investigations.[34] The BIM also requires less computation for updating the weight matrix if the sources and the detectors are not colocated or if there are more detectors than sources. [Note that, when a point source is used, $G(\mathbf{r}_d, \mathbf{r}) = u(\mathbf{r}, \mathbf{r}_s)$ when $\mathbf{r}_d = \mathbf{r}_s$. Therefore, if the sources and the detectors are colocated, no extra calculations are required for updating the Green's function.] A thorough comparison between the BIM and the DBIM in terms of accuracy, robustness, and complexity should be conducted in future studies.

ACKNOWLEDGMENTS

REFERENCES

1. J. Fishkin and E. Gratton, "Propagation of photon-density waves in strongly scattering media containing an absorbing semi-infinite plane bounded by a straight edge," J. Opt. Soc. Am. A **10**, 127–140 (1993).
2. B. J. Tromberg, L. O. Svaasand, T. T. Tsay, and R. C. Haskell, "Properties of photon density waves in multiple-scattering media," Appl. Opt. **32**, 607–616 (1993).
3. D. A. Boas, M. A. O'Leary, B. Chance, and A. G. Yodh, "Scattering of diffuse photon density waves by spherical inhomogeneities within turbid media: analytic solution and applications," Proc. Natl. Acad. Sci. USA **91**, 4887–4891 (1994).
4. E. M. Sevick, B. Chance, J. Leigh, S. Nioka, and M. Maris, "Quantitation of time- and frequency-resolved optical spectra for the determination of tissue oxygenation," Anal. Biochem. **195**, 330–351 (1991).
5. Y. Q. Yao, R. L. Barbour, Y. Wang, H. L. Graber, and J. W. Chang, "Sensitivity studies for imaging a spherical object embedded in a spherically symmetric, two-layer turbid medium with photon-density waves," Appl. Opt. **35**, 735–751 (1996).
6. E. M. Sevick and B. Chance, "Photon migration in a model of the head measured using time- and frequency-domain techniques: potentials of spectroscopy and imaging," in *Time-Resolved Spectroscopy and Imaging of Tissues*, B. Chance and A. Katzir, eds., Proc. SPIE **1431**, 84–96 (1991).
7. S. R. Arridge, "The forward and inverse problems in time resolved infra-red imaging," in *Medical Optical Tomography: Functional Imaging and Monitoring*, G. Mueller, B. Chance, R. Alfano, S. Arridge, J. Beuthan, E. Gratton, M. Kaschke, B. Masters, S. Svanberg, and P. van der Zee, eds., Institute Series of SPIE Optical Engineering (Society of Photo-Optical Instrumentation Engineers, Bellingham, Wash., 1993), pp. 35–64.
8. M. A. O'Leary, D. A. Boas, B. Chance, and A. G. Yodh, "Imaging of inhomogeneous turbid media using diffuse photon density waves," in *Advances in Optical Imaging and Photon Migration*, R. R. Alfano, ed., Vol. 21 of 1994 OSA Proceedings Series (Optical Society of America, Washington, D.C., 1994), pp. 106–115.
9. B. W. Pogue and M. S. Patterson, "Forward and inverse calculations for 3-D frequency-domain diffuse optical tomography," in *Optical Tomography: Photon Migration, and Spectroscopy of Tissue and Model Media: Theory, Human Studies, and Instrumentation*, B. Chance and R. R. Alfano, eds., Proc. SPIE **2389**, 328–339 (1995).
10. Y. Yao, Y. Wang, Y. Pei, W. Zhu, and R. L. Barbour, "Simultaneous reconstruction of absorption and scattering distributions in turbid media using a Born iterative method," in *Experimental and Numerical Methods for Solving Ill-Posed Inverse Problems: Medical and Nonmedical Applications*, R. Barbour, M. Carlin, and M. Fiddy, eds., Proc. SPIE **2570**, 96–107 (1995).
11. Y. Yao, Y. Wang, Y. Pei, W. Zhu, J. Hu, and R. L. Barbour, "Frequency domain optical tomography in human tissue," in *Experimental and Numerical Methods for Solving Ill-Posed Inverse Problems: Medical and Nonmedical Applications*, R. Barbour, M. Carvlin, and M. Fiddy, eds., Proc. SPIE **2570**, 254–266 (1995).
12. M. A. O'Leary, D. A. Boas, B. Chance, and A. G. Yodh, "Simultaneous scattering and absorption images of heterogeneous media using diffusive waves with the Rytov approximation," in *Optical Tomography: Photon Migration, and Spectroscopy of Tissue and Model Media: Theory, Human Studies, and Instrumentation*, B. Chance and R. R. Alfano, eds., Proc. SPIE **2389**, 320–327 (1995).
13. R. L. Barbour, H. L. Graber, Y. Wang, J. Chang, and R. Aronson, "A perturbation approach for optical diffusion tomography using continuous-wave and time-resolved data," in *Medical Optical Tomography: Functional Imaging and Monitoring*, G. Mueller, B. Chance, R. Alfano, S. Arridge, J. Beuthan, E. Gratton, M. Kaschke, B. Masters, S. Svanberg, and P. van der Zee, eds., Institute Series of SPIE Optical Engineering (Society of Photo-Optical Instrumentation Engineers, Bellingham, Wash., 1993), pp. 87–120.
14. S. R. Arridge, P. van der Zee, M. Cope, and D. T. Delpy, "Reconstruction methods for infra-red absorption imaging," in *Time-Resolved Spectroscopy and Imaging of Tissues*, B. Chance and A. Katzir, eds., Proc. SPIE **1431**, 204–215 (1991).
15. Y. M. Wang and W. C. Chew, "An iterative solution of the two-dimensional electromagnetic inverse scattering problem," Int. J. Imaging Syst. Technol. **1**, 100–108 (1989).
16. W. C. Chew and Y. M. Wang, "Reconstruction of two-dimensional permittivity distribution using the distorted Born iterative method," IEEE Trans. Med. Imaging **9**, 218–225 (1990).
17. M. Moghaddadam and W. C. Chew, "Nonlinear two-dimensional velocity profile inversion using time-domain data," IEEE Trans. Geosci. Remote Sens. **30**, 146–156 (1992).
18. N. Joachimowicz, C. Pichot, and J. P. Hugonin, "Inverse scattering: an iterative numerical method for electromagnetic imaging," IEEE Trans. Antennas Propag. **39**, 1742–1752 (1991).
19. A. Ishimaru, *Wave Propagation and Scattering in Random Media* (Academic, New York, 1978), Vol. 1, Chap. 9, pp. 175–190.
20. K. M. Case and P. F. Zweifel, *Linear Transport Theory* (Addison-Wesley, Reading, Mass., 1967), Chap. 8, pp. 194–231.
21. S. A. Arridge, M. Schweiger, M. Hiraoka, and D. T. Delay, "A finite element approach for modeling photon transport in tissue," Med. Phys. **20**, 299–309 (1993).
22. W. L. Briggs, *A Multigrid Tutorial* (Society for Industrial and Applied Mathematics, Philadelphia, Pa., 1987).
23. W. Hackbusch, *Multi-Grid Methods and Applications* (Springer-Verlag, New York, 1985).
24. R. E. Alcouffe, A. Brandt, J. E. Dendy, and J. W. Painter, "The multi-grid method for the diffusion equation with strongly discontinuous coefficients," SIAM (Soc. Ind. Appl. Math.) J. Sci. Stat. Comput. **2**, 430–454 (1981).
25. R. Fulton, C. E. Ciesielski, and W. H. Schubert, "Multigrid methods for elliptic problems: a review," Mon. Weather Rev. **114**, 943–959 (1986).
26. J. C. Adams, "MUDPACK: multigrid portable FORTRAN software for the efficient solution of linear elliptic partial differential equation," Appl. Math. Comput. **34**, 113–146 (1989).
27. A. N. Tikhonov and V. Y. Arsenin, *Solutions of Ill-Posed Problem* (V. H. Winston, Washington, D.C., 1977).
28. W. W. Zhu, Y. Wang, R. L. Barbour, H. L. Graber, and J. Chang, "Regularized progressive expansion algorithm for recovery of scattering media from time-resolved data," in *Advances in Optical Imaging and Photon Migration*, R. R. Alfano, ed., Vol. 21 of 1994 OSA Proceedings Series (Optical Society of America, Washington, D.C., 1994), pp. 211–216.
29. R. L. Barbour, H. L. Graber, R. Aronson, and J. Lubowsky, "Model for 3-D optical imaging of tissue," in *Proceedings of the IEEE 10th Annual International Geoscience and Remote Sensing Symposium* (Institute of Electrical and Electronics Engineers, New York, 1990), pp. 1395–1399.
30. R. L. Barbour, H. L. Graber, R. Aronson, and J. Lubowsky, "Imaging of subsurface regions of random media by remote sensing," in *Time-resolved Spectroscopy and Imaging of Tissues*, B. Chance, ed., Proc. SPIE **1431**, 192–203 (1991).
31. J. R. Singer, F. A. Grunbaum, P. Kohn, and J. P. Zubelli, "Image reconstruction of the interior of bodies that diffuse radiation," Science **248**, 990–993 (1990).

32. *Optical Tomography: Photon Migration, and Spectroscopy of Tissue and Model Media: Theory, Human Studies, and Instrumentation*, B. Chance and R. R. Alfano, eds., Proc. SPIE **2389** (1995).
33. S. A. Arridge, M. Schweiger, M. Hiraoka, and D. T. Delay, "Performance of an iterative reconstruction algorithm for near infrared absorption and scatter imaging," in *Photon Migration, and Imaging in Random Medium and Tissues*, Proc. SPIE **1888**, 360–371 (1993).
34. Y. Q. Yao, "Forward and inverse studies for optical image reconstructions," Ph.D. dissertation (Polytechnic University, Brooklyn, N.Y., 1996).